Laser-resonance Lamb-shift measurement in hydrogenlike phosphorus

P. Pellegrin,* Y. El Masri, and L. Palffy†

Institut de Physique Nucléaire, Université Catholique de Louvain, 2 Chemin du Cyclotron, B-1348 Louvain-la-Neuve, Belgium

(Received 18 June 1984)

We report our final result on the Lamb-shift measurement in hydrogenlike phosphorous using the $2s_{1/2}$-$2p_{3/2}$ laser-resonance method. From the measured value of the $2s_{1/2}$-$2p_{3/2}$ energy splitting [539.60(20) THz, or 5555.8(2.0) Å] the Lamb shift S is deduced in the framework of Erickson's and Mohr's calculations. S_{expt}^{E} and S_{expt}^{M} are the results of the subtraction of the measured $2s_{1/2}$-$2p_{3/2}$ energy splitting and the fine structure calculated by the two authors, respectively. The results, $|S_{E}-S_{\text{expt}}^{E}|=0.43\pm0.20$ THz and $|S_{M}-S_{\text{expt}}^{M}|=0.12\pm0.20$ THz, indicate agreement with Mohr's theoretical approach (S_{M}) and are more than two standard deviations from Erickson's calculations (S_{E}). A general overview on the experimental techniques and results is given. The general trend of the presently available experimental results on Lamb-shift measurements are compared with Mohr's calculations.

I. INTRODUCTION

In a previous Letter[1] we reported our preliminary result on the Lamb-shift measurement in hydrogenlike phosphorus using the $2s_{1/2}$-$2p_{3/2}$ laser-resonance-quenching method by means of a high-power nitrogen-pumped dye laser. The experiment having been completed, we report the final result including additional data subsequently obtained using the same experimental setup. In fact, since the earlier published value[1] of 5556.5(2.5) Å or 539.53(25) THz for the $2s_{1/2}$-$2p_{3/2}$ energy splitting in the hydrogenlike phosphorus, two additional resonance curves have been measured, resulting in a more accurate result.

In this paper we give a detailed description of our experiment. In Sec. II we compare Erickson's and Mohr's calculations pointing out the relevant discrepancies and agreements between the two approaches. Section III describes the general philosophy of the experiment and the main properties of the studied ion. In Sec. IV we detail the experimental difficulties encountered and their solutions. Our final result is discussed in Sec. V where we also give an overview of the presently available experimental data on Lamb shift and comment on their general trend in comparison to the quantum electrodynamic calculations.

II. THE HYDROGENLIKE ATOM

A. The Dirac atom

Although a complete covariant description of bound systems is in principle possible using the Bethe-Salpeter[2] equation, it is generally more appropriate to describe such systems by means of a more simple equation completed by additional corrections.

The hydrogenlike atomic structure is usually described (Dirac picture) as a pointlike nonrelativistic nucleus of charge (Ze) on its mass shell, surrounded by a pointlike electron of charge e, spin $\frac{1}{2}$, and reduced mass μ interacting with the nuclear classical Coulomb field. Then the energy levels calculated from the Dirac equation[3] are

$$E_{D\mu}=\mu c^{2}\left[1+\left[\frac{Z\alpha}{n-\epsilon}\right]^{2}\right]^{-1/2}-\mu c^{2}, \qquad (1)$$

where $\alpha=1/137.035\,95(12)$ (Ref. 4) is the fine-structure constant, Z is the nuclear charge number, $\mu=mM/(m+M)$ is the reduced mass, m and M are the electron and the nucleus rest mass, respectively, $n=1,2,\ldots$ the principal quantum number, and $\epsilon=j+\frac{1}{2}-[(j+\frac{1}{2})^{2}-(Z)^{2}]^{1/2}$ the quantum defect with $j=\frac{1}{2},\frac{3}{2},\ldots$ the level total angular momentum. The zero energy corresponds to the completely ionized ion; all bound states are of negative energies.

The fine-structure splitting $\Delta E\,(2p_{3/2}$-$2p_{1/2})$ is then expressed as

$$\Delta E=\mu c^{2}\left\{\left[1-\left[\frac{Z\alpha}{2}\right]^{2}\right]^{1/2}\right.$$
$$\left.-\left[\frac{1+[1-(Z\alpha)^{2}]^{1/2}}{2}\right]^{1/2}\right\}, \qquad (2)$$

the $2s_{1/2}$ and $2p_{1/2}$ levels being degenerate. However, radiative corrections remove this degeneracy resulting in the so-called "Lamb-shift splitting" between the $2s_{1/2}$ and $2p_{1/2}$ levels.

B. Lamb shift in hydrogen and hydrogenic atoms

The first calculation of the Lamb shift, based on the nonrelativistic formulation of the radiation theory, was performed by Bethe[5] (1947) and yielded a good order of magnitude of the $2s_{1/2}$-$2p_{1/2}$ splitting in hydrogen. Based on quantum electrodynamics, Erickson and Yennie[6] (1965), Erickson,[7,8] and Mohr[9-13] made more detailed calculations of the radiative corrections for higher Z ions and higher principal quantum number (n).

In spite of this lengthy and elaborate development, a basic disagreement remains in the theoretical estimations of the most important contribution to the Lamb shift, the electron self-energy. These discrepancies could not be

TABLE I. Contributions of the electron self-energy to the Lamb shift following Erickson's approach. This table details analytically the coefficients in Eq. (5) (see text), where $C_{lj} = 1/l + 1$, $j = l + \frac{1}{2}$ and $-1/l$, $j = l - \frac{1}{2}$; $\ln K_0(2,0)$ and $\ln K_0(2,1)$ are the Bethe logarithms of the $2s$ and $2p$ levels; $\ln K_0(2,0) = -2.811769\ldots$; $\ln K_0(2,1) = +0.030017\ldots$; $\delta_{l_0} = 0$ for p states ($l = 1$) and 1 for s states ($l - 0$).

Coefficient	
A_{40}	$\frac{4}{3}\left[(\frac{11}{24}\delta_{l_0}) + \ln K_0(2,\delta_{l_1}) + \frac{3}{8}\frac{C_{lj}}{(2l+1)}\right]$
A_{41}	$\frac{4}{3}\delta_0$
A_{50}	$\frac{4}{3}[3\pi(1 + \frac{11}{128} - \frac{1}{2}\ln 2)\delta_{l_0}]$
A_{60}	$\frac{4}{3}[-17.598\delta_{l_0} + (-0.352\delta_{j1/2} - 0.438\delta_{j3/2})(1 - \delta_{l_0})]$
A_{61}	$\frac{4}{3}\left[(4\ln 2 + \frac{201}{120})\delta_{l_0} + (103\delta_{j1/2} + 58\delta_{j3/2})\frac{(1-\delta_{l_0})}{240}\right]$
A_{62}	$\frac{4}{3}(-\frac{3}{4}\delta_{l_0})$
A_{70}	$\frac{4}{3}[18.48\delta_{l_0} + (-1.28\delta_{j1/2} - 0.32\delta_{j3/2})(1 - \delta_{l_0})]$

clearly resolved in the hydrogen atom in spite of extraordinary precise experimental measurements.

This difficulty in the hydrogen atom originates from additional corrections such as the reduced mass, the relativistic recoil, and the nuclear size, whose contributions to the splitting are more important than the disagreement between Erickson's and Mohr's self-energy estimates. In fact the previous predictions of Erickson and Mohr for the Lamb shift in hydrogen were

$$S_E = 1057.910 \pm 0.010 \text{ MHz},$$

$$S_M = 1057.867 \pm 0.013 \text{ MHz}.$$

But if corrected to take into account a recent measurement of the mean-square radius of the proton,[14] these results become

$$S_E = 1057.934 \pm 0.010 \text{ MHz},$$

$$S_M = 1057.888 \pm 0.014 \text{ MHz}.$$

One observes that the new value of this external parameter introduces a change in the Lamb shift which is half the disagreement with Erickson's and Mohr's calculations.

On the other hand, the last two experimental results, $S_{LP} = 1057.845 \pm 0.009$ MHz (Ref. 15) and $S_{SY} = 1057.8594 \pm 0.0019$ MHz (Ref. 16) seem to be closer to Mohr's result but remain significantly in disagreement with each other and with the theory.

Only Sapirstein's theoretical result[17] $S_S = 1057.860(9)$ MHz seems to be in agreement with the experimental values. No information, however, is available for the finite size and the reduced-mass corrections used in these calculations.

Because of the severe Z dependence of the radiative corrections ($\sim Z^4$), the confrontation between theory and experiment in higher Z ions would be a better test of the QED theory. Therefore, we compile Erickson's and Mohr's estimates for the various contributions to the Lamb shift in different Z ions.

C. Self-energy

Following QED, the electron self-energy (SE) contribution to the atomic level shift can be written in a dual series expansion having the form

$$\delta E_{SE} = \sum_{i=1}^{\infty} \sum_{j=4}^{\infty} B_{ij} \alpha^i (Z\alpha)^j . \tag{3}$$

The main contribution to the Lamb shift for the $n = 2$ levels is expressed as the lowest power in α ($i = 1$) of this expansion,

$$\delta E_{SE}(Z\alpha) = \frac{\alpha}{\pi} \frac{(Z\alpha)^4}{8} mc^2 F(Z\alpha) . \tag{4}$$

In this expression, $F(Z\alpha)$ is a state-dependent series.

First, Erickson and Yennie[6] introduced an original operator technique to calculate the $F(Z\alpha)$ series up to the order $(Z\alpha)^2$ in agreement with previous calculations. Later, Erickson[7,8] estimated the contributions up to the $(Z\alpha)^3$ term. He expressed $F(Z\alpha)$ as

$$F(Z\alpha) = \{A_{40} + A_{41}\ln[(Z\alpha)^{-2}]\} + A_{50}Z\alpha$$

$$+ \{A_{60} + A_{61}\ln[(Z\alpha)^{-2}]$$

$$+ A_{62}\ln^2[(Z\alpha)^{-2}]\}(Z\alpha)^2$$

$$+ A_{70}(Z\alpha)^3 . \tag{5}$$

The coefficient A_{70} is assumed to contain all higher-order contributions. Table I shows the details of the coefficients in expression (5).

Proceeding differently, Mohr[9-13] estimated numerically the $F(Z\alpha)$ function for the $1s_{1/2}$, $2s_{1/2}$, $2p_{1/2}$, and $2p_{3/2}$ states. From these results one deduces the $2s_{1/2}$-$2p_{1/2}$ Lamb shift as

$$S_{SE}(Z\alpha) = \delta E_{SE}(2s_{1/2}) - \delta E_{SE}(2p_{1/2})$$

which can be displayed, for convenience, in a closed form similar to Eq. (5):

$$S_{SE} = \frac{4}{3}\frac{\alpha}{\pi}\frac{(Z\alpha)^4}{8}mc^2\left[\ln[(Z\alpha)^{-2}] + \ln\left[\frac{K_0(2,0)}{K_0(2,1)}\right] + \frac{11}{24} + \frac{1}{2} + 3\pi(1 + \frac{11}{128} - \frac{1}{2}\ln 2)Z\alpha\right.$$

$$\left. - \frac{3}{4}(Z\alpha)^2\ln^2[(Z\alpha)^{-2}] + (\frac{299}{240} + 4\ln 2)(Z\alpha)^2\ln[(Z\alpha)^{-2}] + (Z\alpha)^2 G_{SE}(Z\alpha)\right] . \tag{6}$$

TABLE II. Residual contributions of the electron self-energy to the Lamb shift following Mohr's approach. Numerical values of the G_{SE} function for $Z=1$ and for $9 \leq Z \leq 20$ (see text).

Z	A	$G_{SE}(Z\alpha)$
1	1	$-23.4(1.2)$
9	19	$-20.42(39)$
10	20	$-20.13(34)$
11	23	$-19.85(29)$
12	24	$-19.58(24)$
13	27	$-19.31(20)$
14	28	$-19.06(17)$
15	31	$-18.81(14)$
16	32	$-18.57(11)$
17	35	$-18.338(84)$
18	40	$-18.111(63)$
19	39	$-17.890(44)$
20	40	$-17.674(38)$

TABLE III. Residual contributions of the vacuum polarization effect to the Lamb shift following Mohr's calculations. Numerical values of the $G_U(Z\alpha)$ function for $Z=1$ and $9 \leq Z \leq 20$ hydrogenlike atoms.

Z	A	$G_U(Z\alpha)$
1	1	-0.5587
9	19	-0.5059
10	20	-0.5015
11	23	-0.4974
12	24	-0.4936
13	27	-0.4900
14	28	-0.4867
15	31	-0.4836
16	32	-0.4807
17	35	-0.4781
18	40	-0.4756
19	39	-0.4733
20	40	-0.4711

This expression does not take into account the coefficients A_{60} and A_{70} as estimated by Erickson and Yennie. However, a similar closed contribution is included assuming $G_{SE}(Z\alpha)=a+bZ\alpha\ln[(Z\alpha)^{-2}]+cZ\alpha$. In order to evaluate the coefficients a, b, and c, the Lamb shifts for $Z=10,20,\ldots,110$ were calculated numerically. The results for the other values of Z are then deduced by interpolation or extrapolation methods. This approach will be discussed in more detail in the last section of this paper in connection with the experimental data. In Table II we give the values of G_{SE} for $Z=1$ and for $9 \leq Z \leq 20$; a complete tabulation is given in Ref. 13.

D. Vacuum polarization

Deduced first by Serber and Uehling in 1935, the vacuum polarization (VP) modifies the Coulomb potential $V(r)$ at short distances: $V(r) \rightarrow V(r) + \delta V(r)$. Later, Erickson combined his results with an additional correction introduced by Wichmann and Kroll[18] (see also Ref. 12) to express the VP-level-shift contribution as

$$\delta E_{VP} = \frac{4}{3}\frac{\alpha}{\pi}\frac{(Z\alpha)^4}{8}mc^2$$

$$\times\{[H_U(Z\alpha)+(Z\alpha)^2 H_{WK}(Z\alpha)]\delta_{l0}\}, \qquad (7)$$

where $H_{WK}(Z\alpha)=0.042\,51-0.103\,05Z\alpha$ and

$$H_U(Z\alpha)=\{-\tfrac{1}{5}+\tfrac{5}{64}\pi Z\alpha-0.1(Z\alpha)^2\ln[(Z\alpha)^{-2}]$$

$$-\tfrac{9}{35}(Z\alpha)^2+\tfrac{21}{256}\pi(Z\alpha)^3\},$$

$$\delta_{l0}=\begin{cases}0, & \text{for } p \text{ states } (l=1) \\ 1, & \text{for } s \text{ states } (l=0).\end{cases}$$

Mohr estimated numerically the $H_U(Z\alpha)$ function and, for convenience, displayed the VP contribution as

$$S_{VP}=\frac{4}{3}\frac{\alpha}{\pi}\frac{(Z\alpha)^4}{8}mc^2$$

$$\times\{-\tfrac{1}{5}+\tfrac{5}{64}\pi Z\alpha-0.1(Z\alpha)^2\ln[(Z\alpha)^{-2}]$$

$$+(Z\alpha)^2[G_U(Z\alpha)+H_{WK}(Z\alpha)]\}, \qquad (8)$$

where $G_U(Z\alpha)$ function is tabulated for $Z=1$ and $9 \leq Z \leq 20$ in Table III. It is to be noted that there are no significant differences between Eqs. (7) and (8).

E. Reduced-mass effect

The reduced-mass contribution (RM) to the Lamb shift is not an additional correction but is normally introduced in the SE and VP contributions. For convenience it is considered as a separate term and takes the following form in lowest order:

$$\delta E_{RM}=\frac{4}{3}\frac{\alpha}{\pi}\frac{(Z\alpha)^4}{8}mc^2\left[-3\frac{m}{M}\right]$$

$$\times\left[\ln[(Z\alpha)^{-2}]+\tfrac{11}{24}-\tfrac{1}{5}+\ln K_0(2,0)\right.$$

$$\left.+\frac{3}{8}\frac{C_{lj}}{2l+1}\right] \qquad (9)$$

for the 2s state and

$$\delta E_{RM}=\frac{4}{3}\frac{\alpha}{\pi}\frac{(Z\alpha)^4}{8}mc^2\left[-2\frac{m}{M}\right]$$

$$\times\left[\tfrac{3}{2}\ln K_0(2,1)+\frac{3}{8}\frac{C_{lj}}{2l+1}\right] \qquad (10)$$

for the $2p_{1/2}$ and $2p_{3/2}$ states. The RM contribution is

deduced from Eqs. (9) and (10) with $m \ll M$ (the nucleus mass):

$$S_{RM} = \frac{4}{3} \frac{\alpha}{\pi} \frac{(Z\alpha)^4}{8} mc^2 \left[-3\frac{m}{M} \right]$$

$$\times \left[\ln[(Z\alpha)^{-2}] + \ln\left[\frac{K_0(2,0)}{K_0(2,1)} \right] + \frac{23}{60} \right] . \quad (11)$$

No significant disagreement exists between Erickson and Mohr at this point. However this contribution can be neglected for $Z > 10$.

F. Fourth- (and higher-) order contributions

Erickson's α^2 [fourth-order (FO)] contribution to the level shift is

$$\delta E_{FO} = \frac{4}{3} \left[\frac{\alpha}{\pi} \right]^2 \frac{(Z\alpha)^4}{8} mc^2$$

$$\times \left[0.650\,565\delta_{l0} - 0.246\,359\frac{C_{lj}}{2l+1} \right] . \quad (12)$$

It contributes to the Lamb shift by an amount

$$S_{FO} = \frac{4}{3} \left[\frac{\alpha}{\pi} \right]^2 \frac{(Z\alpha)^4}{8} mc^2 \times 0.322\,086 . \quad (13)$$

The effect of higher orders in α $(\alpha^3, \dots)$ have been shown[6] to give no significant contribution to the Lamb shift and can always be neglected.

G. Relativistic recoil effect

The Bethe-Salpeter equation[2] describing the hydrogenic ion gives an additional term to the Lamb shift, which must be separately included as a correction to the Dirac equation. At the lowest power in (m/M), the induced level shift can be written as

$$\delta E_{RR} = \frac{4}{3} \frac{\alpha}{\pi} \frac{(Z\alpha)^4}{8} mc^2 \left[Z\frac{m}{M} \right]$$

$$\times \left[2(\{ \ln[(Z\alpha)^{-2}] + \tfrac{11}{24} \}\delta_{l0} + \ln K_0(2,\delta_{l1})) \right.$$

$$- \frac{7}{2} \left[\{ \tfrac{1}{2}\ln[(Z\alpha)^{-2}] - \tfrac{9}{4} \}\delta_{l0} \right.$$

$$\left. + \frac{1-\delta_{l0}}{2l(l+1)(2l+1)} \right] - \delta_{l0} \right] . \quad (14)$$

This gives the relativistic recoil (RR) Lamb-shift contribution

$$S_{RR} = \frac{4}{3} \frac{\alpha}{\pi} \frac{(Z\alpha)^4}{8} mc^2 \left[Z\frac{m}{M} \right]$$

$$\times \left[\tfrac{1}{4}\ln[(Z\alpha)^{-2}] + 2\ln\left[\frac{K_0(2,0)}{K_0(2,1)} \right] + \frac{97}{12} \right] . \quad (15)$$

H. Nuclear size

The finite size of the nucleus (NS) contributes to the Lamb shift and can be estimated separately. Assuming a spherical nucleus, Erickson obtained, for the $2s$ and $2p$ levels, respectively,

$$\delta E^s_{NS} = \frac{4}{3} \frac{\alpha}{\pi} \frac{(Z\alpha)^4}{8} mc^2 \frac{\pi}{2\alpha} \frac{\langle R^2 \rangle}{\lambda_e^2}(1+C) , \quad (16)$$

$$\delta E^p_{NS} = \frac{4}{3} \frac{\alpha}{\pi} \frac{(Z\alpha)^4}{8} mc^2 \frac{\pi}{2\alpha} \frac{\langle R^2 \rangle}{\lambda_e^2} \frac{10}{7} \frac{\langle R^2 \rangle}{a^2} , \quad (17)$$

where $a = 2\hbar/Z\alpha mc$ is the Bohr radius $(n=2)$, $\langle R^2 \rangle$ is the nucleus quadratic radius, and $C = -0.004$ for $Z=1$, $C = -0.147$ for $Z \neq 1$. It clearly appears that the $2s$ contribution dominates over the $2p$ one with

$$\delta E_{NS}(2s) \simeq 10^6 \delta E_{NS}(2p) .$$

Mohr obtained a different result for the (NS) contribution

$$S_{NS} = \frac{4}{3} \frac{\alpha}{\pi} \frac{(Z\alpha)^4}{8} mc^2 \frac{\pi}{2\alpha} \left[[(Z\alpha)^{-2}+1.70] \left[\frac{Z\alpha R}{\lambda_e} \right]^{2s} \right] , \quad (18)$$

where $s = [1-(Z\alpha)^2]^{1/2}$. This result is significantly different from Erickson's one which can be deduced from Eqs. (16) and (17). The relative difference is 0.47% at $Z=1$, 30% at $Z=15$, and 71% for $Z=30$.

I. Total Lamb-shift splitting

The total Lamb shift can be written as the sum of all the individual contributions previously detailed:

$$S = S_{VP} + S_{SE} + S_{FO} + S_{RM} + S_{RR} + S_{NS} . \quad (19)$$

Erickson's and Mohr's estimates differ by S_{VP}, S_{SE}, and S_{NS} terms. However, Mohr adopted in his calculations the S_{FO}, S_{RM}, and S_{RR} contributions following the predictions of Erickson.

Table IV shows as an example these different contributions to the Lamb shift in three hydrogenlike atoms $Z=1$, 15, and 30. In this table one can see in column $|E-M|$ the difference between Erickson's and Mohr's calculations, hence the precision required experimentally in order to discriminate between the two approaches. In the case of hydrogen $(Z=1)$ this precision must be of the order of 43 ppm; in phosphorus, 1.5% and only 6.6% in zinc. These indications clearly show the interest of the Lamb-shift measurements in high-Z atoms.

J. Radiative corrections to the fine structure

The energy splitting $\Delta E(2p_{3/2}\text{-}2p_{1/2})$ introduced in Eq. (2) must be amended by taking into account the radiative corrections. Following Erickson,[8] these contributions can be written as

TABLE IV. Details of the Lamb-shift estimates in three hydrogenlike atoms $Z = 1$, 15, and 30 following Erickson's and Mohr's prescriptions. R and M values for the $Z = 15$ and 30 are extracted from Mohr's tabulations in Ref. 10, while R (hydrogen) is taken from Ref. 14; $\alpha^{-1} = 137.035\,965(12)$ is taken from Ref. 4 (see text for detailed discussions).

	Hydrogen $Z = 1$ (MHz)			Phosphorus $Z = 15$ (THz)			Zinc $Z = 30$ (THz)		
	Erickson	Mohr	$|E-M|$	Erickson	Mohr	$|E-M|$	Erickson	Mohr	$|E-M|$
Self-energy	1085.859	1085.814	0.045	21.700	21.394	0.306	254.27	239.23	15.04
Vacuum polarization	−26.895	−26.897	0.002	−1.244	−1.262	0.018	−18.73	−19.94	1.21
Higher order (α^2)	0.102	0.102		0.005	0.005		0.08	0.08	
Reduced mass	1.636	−1.636		−0.001	−0.001		−0.00	−0.00	
Relativistic recoil	0.359	0.359		0.006	0.006		0.09	0.09	
Nuclear size	0.145	0.146	0.001	0.086	0.112	0.026	2.11	3.54	1.44
Total	1057.934(10)	1057.888(14)	0.046 43 ppm	20.553(62)	20.254(12)	0.299 1.5%	237.8(3.8)	223.00(20)	14.8 6.6%
Nuclear parameters	$R = 0.862(12)$ fm $M = 1.007276$ a.u.			$R = 3.19(1)$ fm $M = 30.97$ a.u.			$R = 3.96(3)$ fm $M = 63.91$ a.u.		

$$\Delta E = \mu c^2 \left\{ \left[1 - \left[\frac{Z\alpha}{2} \right]^2 \right]^{1/2} - \left[\frac{1 + [1 - (Z\alpha)^2]^{1/2}}{2} \right]^{1/2} \right\} + \frac{4}{3} \frac{\alpha}{\pi} \frac{(Z\alpha)^4}{8} mc^2 \frac{3}{16}$$

$$\times \left[\left[\frac{\mu}{m} \right]^2 - (Z\alpha)^2 \ln[(Z\alpha)^{-2}] + 4(\Delta A_{60} + \Delta A_{70}) + 2\frac{\alpha}{\pi}(-0.328) \right] . \tag{20}$$

Mohr's fine-structure estimates can be extracted from the previous equations (4), (8), (10), (12), (14), (17) and the related tables (see also Ref. 10).

K. Hyperfine structures

The energy splitting induced by the hyperfine interaction results from the coupling between the nuclear magnetic moment (μ) of the atomic nucleus with spin(I) and the magnetic moment of the electron. Thus in hydrogenlike atoms, for each atomic level described by the quantum number (n, j, and l), the hyperfine energy separation of the most separated substates can be expressed as

$$\Delta E_{HF} = \frac{m}{M_p} \frac{4}{n^3} \frac{Z^3 \alpha^3 g}{(2l+1)(j+1)} R_y$$

$$\times \begin{cases} I + \frac{1}{2}, & j \leq I \\ I(j+1/2)/j, & j \geq I \end{cases} \tag{21}$$

where $g = \mu/I$ is the nuclear gyromagnetic ratio expressed in nuclear magnetons, M_p the proton mass, and $R_y = 13.605\,804$ eV, the Rydberg constant. Although these substates, described by the hyperfine coupling $\vec{F} = \vec{I} + \vec{j}$, are shifted with respect to the unperturbed positions by the amount

$$\delta E = Ct \left[F(F+1) - I(I+1) - j(j+1) \right] ,$$

their level centroids remain unaffected.

III. PHILOSOPHY OF THE EXPERIMENT

A. Introduction

The experimental techniques used in the Lamb-shift measurements in high-Z atoms are different from those in light elements $(Z = 1,2,3)$. In such cases the production of hydrogenic ions in the $2s_{1/2}$ level cannot be achieved by electronic bombardment, and one needs heavy-ion accelerators combined with the well-known beam-foil technique. The order of magnitude of the ion energy is of several MeV per nucleon. On the other hand, for $Z \geq 4$ the classical rf resonance techniques cannot be applied because of the limitation in frequency and in power. Three other methods are usually employed: (i) The Stark-quenching technique, where one measures the lifetime of the mixed $2s_{1/2}$-$2p_{1/2}$ state in a known electric field, (ii) The laser-resonance technique, where the $2s_{1/2} \rightarrow 2p_{1/2}$ or the $2s_{1/2} \rightarrow 2p_{3/2}$ transition is induced by means of a tunable laser and monitored by the detection of the subsequent Lyman-α x rays. The Stark-quenching technique suffers from possible systematic effects due to changes in

the ion trajectory, to the presence of unresolved background contribution, and to cascading effects feeding the $2s_{1/2}$ level during the flight. These types of difficulties are not present in the laser-resonance technique, which in contrast lies on the limitation of the technology and suffers from alignment problems. (iii) The electric field anisotropy technique, where the anisotropy of the emitted x rays is measured when the $2s_{1/2}$ and $2p_{1/2}$ states are mixed by an electric field. This method seems to be very promising and allows the extension of the Lamb-shift measurements to higher Z.[19] Using this approach[20] the Lamb shift in deuterium and oxygen have been measured with high precision. We have, however, chosen the laser-resonance method and in the following we will show that it is well adapted for several candidates with atomic numbers $Z < 20$.

B. Principle of the measurement

The energy levels of hydrogenlike atoms of interest herein are shown in Fig. 1.

1. The $2s_{1/2}$ state

The parity selection rules between atomic states forbid the $E1$ transition between $2s_{1/2}$ and $1s_{1/2}$ ground state. Likewise the small energy splitting S (LS) between $2s_{1/2}$ and $2p_{1/2}$ also inhibits the $E1$ transition between these two states. Thus the $2s_{1/2}$-state lifetime is essentially induced by the two-photon $2E1(2s_{1/2} \rightarrow 1s_{1/2})$ transition and the $M1(2s_{1/2} \rightarrow 1s_{1/2})$ allowed transition by the relativistic effects.

Parpia and Johnson[21] have recently calculated the decay rate of the $2s_{1/2}$ state. For $Z \sim 15$ this estimate can be written as

$$\gamma_{2s} \approx 8.15 Z^6 \, (2E1) + 2.53 \times 10^{-6} Z^{10} \, (M1) \, s^{-1} , \quad (22)$$

where the numerical coefficients are also Z dependent.

2. The $2p_{1/2}$ and $2p_{3/2}$ lifetimes

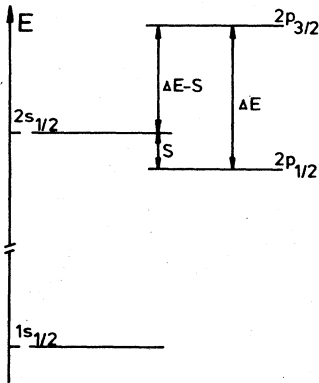The dipole approximation of the $E1$ transition between the $2p$ states and the ground state can be expressed by

FIG. 1. Partial energy-level diagram of hydrogenic atoms.

$$\gamma_{2p} = 6.265 \times 10^8 Z^4 \, s^{-1} . \quad (23)$$

This approximate value is within 2% of Mohr's calculations[4] based on QED theory.

The metastability of the $2s_{1/2}$ level is exploited to induce resonant transitions to the $2p_{1/2}$ or $2p_{3/2}$ levels. The experiment consists of counting the number of Lyman α x rays as a function of the wavelength of the laser light interacting with the ion beam. The centroid of the measured Lorentzian shape corresponds to the energy splitting of the coupled levels.

If the decay rate of the $2s_{1/2}$ level is considered to be negligible compared to the deexcitation rate of the $2p$ level ($\gamma_{2s} \ll \gamma_{2p}$), the probability ($p$) of the $2s \rightarrow 2p$ transition is given by[22,23]

$$p = \frac{\gamma_R}{\gamma_{2s} + \gamma_R} \{ 1 - \exp[-(\gamma_{2s} + \gamma_R)T] \} , \quad (24)$$

where T is the interacting time of the ion and the laser beams, and

$$\gamma_R = f \frac{9\alpha}{2\pi\hbar} \left[\frac{a_0}{Z} \right]^2 I_0 \frac{\gamma_{2p}}{(\nu - \nu_0)^2 + (\gamma_{2p}/4\pi)^2} .$$

Here, f is given by the selection rules $f = \frac{2}{3}$ for $2s_{1/2} \rightarrow 2p_{3/2}$ and $\frac{1}{3}$ for $2s_{1/2} \rightarrow 2p_{1/2}$, a_0 is the Bohr radius, I_0 the power density of the laser (W/cm^2), and ν_0 the expected resonance frequency. In the case of perpendicular laser-ion beams, T is very short (typically of order 10^{-10} s) so that Eq. (24) can be simplified to

$$p = \gamma_R T . \quad (25)$$

The shape of the resonance is Lorentzian, with a full width at half maximum (FWHM) of

$$\Gamma_{nat} \equiv \frac{\gamma_{2p}}{2\pi}$$

depending only on the $2p$-state lifetime or natural width. In the presence of hyperfine structure

$$p = \sum_j p_j , \quad (26)$$

where p_j is an expression similar to that of Eq. (25) but written for each specific hyperfine transition. In the case of statistically populated hyperfine sublevels, the frequency of the resonance is not shifted, but only slightly broadened.

The quality factor Q of a resonance can be defined as the ratio of the energy splitting to the transition width:

$$Q = \frac{S}{\hbar\gamma_{2p}} \sim F(Z\alpha) \sim 4$$

for the $2s_{1/2}$-$2p_{1/2}$ case and

$$Q = \frac{\Delta E - S}{\hbar\gamma_{2p}} \sim \frac{\Delta E}{\hbar\gamma_{2p}} \sim 110$$

for the $2s_{1/2}$-$2p_{3/2}$ transition. As a consequence the tuning of the $2s_{1/2}$-$2p_{3/2}$ resonance is easier experimentally. However, the relative precision of the extracted value of the Lamb shift is not increased because it is obtained by

TABLE V. The properties and parameters of interest of the atomic energy diagram of the hydrogenic phosphorus.

| | Phosphorus $Z=15$ | | |
	Erickson	Mohr	
ΔE	2.314 788(96)	2.314 877(30)	.eV
S	0.084 947(250)	0.083 764(54)	eV
$\Delta E - S$	2.229 838(270)	2.231 113(62)	eV
	5560.3(6)	5557.10(15)	$\overset{\circ}{A}$

Nucleus spin $I = \frac{1}{2}$, g factor $= 1.1305$
$\Delta E_{HF}(2s_{1/2}) = 243$ GHz $= 0.001$ eV
$\Delta E_{HF}(2p_{3/2}) = 32$ GHz $= 0.000 13$ eV

$\gamma_{2s} = 9.62 \times 10^7$ s^{-1}; $\tau_{2s} = \gamma_{2s}^{-1} = 10.4 \times 10^{-9}$ s
$\gamma_{2p} = 3.16 \times 10^{13}$ s^{-1}; $\tau_{2p} = \gamma_{2p}^{-1} = 3.16 \times 10^{-14}$ s

Natural width of the resonance
$\Gamma_{nat} = \gamma_{2p}/2\pi = 5.03 \times 10^{12}$ Hz $\rightarrow 0.0208$ eV $\rightarrow 51.8$ $\overset{\circ}{A}$

---

subtracting the measured $(\Delta E - S)$ value from the calculated fine structure ΔE.

Owing to problems related to the ion sources in the heavy-ion accelerators, and to the lack of adequate laser systems, there are only a few candidates for a Lamb-shift measurement using the laser-resonance method $(9 \leq Z \leq 20)$. Some experiments of this type have already been performed or are in progress in $Z = 9, 17$ or started in $Z = 16$ systems. The theoretical $(\Delta E - S)$ splittings of Si $(Z = 14)$, P $(Z = 15)$, and S $(Z = 16)$ are, respectively, 7344, 5560, and 4286 Å, implying the possibility of tuning the $(\Delta E - S)$ resonance in a continuous way by means of an appropriate dye laser.

We finally undertook the Lamb-shift measurement in the hydrogenic phosphorus ion, in spite of the important difficulties in producing the ion beam in the accelerator using the explosive and poisonous gas PH$_3$. In Table V are listed the properties of interest of the involved atomic levels of hydrogenic phosphorus.

In conclusion, the Lamb shift in hydrogenlike phosphorus was measured using the $2s_{1/2}$-$2p_{3/2}$ laser-resonance method by means of a tunable and pulsed high-power dye laser. The pulsed structures of both the laser beam and the ion beam delivered by the cyclotron of Louvain-la-Neuve were exploited in order to enhance the signal-to-background ratio. The difficulties encountered, and their adopted solutions, are described in the following section.

IV. EXPERIMENTAL SETUP

A. General description of the experimental setup

A typical 1 μA current of P^{5+} ions of 87.1 MeV was extracted from the isochronous cyclotron of Louvain-la-Neuve. Bare P^{15+} ions, produced in a (1 cm $\times$ 2 cm) carbon foil (C$_1$) 100 μg/cm^2 thick (see Fig. 2), are selected with the steering magnet of the cyclotron and made incident upon a second carbon-adder foil (C$_2$) to produce hydrogenic phosphorus P^{14+} ions ($\sim$20 nA) of which

part are in the metastable $2s_{1/2}$ state. A complete charge-state analysis and detailed spectroscopic work have already been reported.[24-27]

The ion beam was shaped by slits and antiscattering collimators to a spot of 1 mm(V) $\times$ 30 mm(H) in the interaction region with the laser. The ion-beam direction and shape were monitored by two dual grip-type beam scanners[28] placed before and after the interaction region
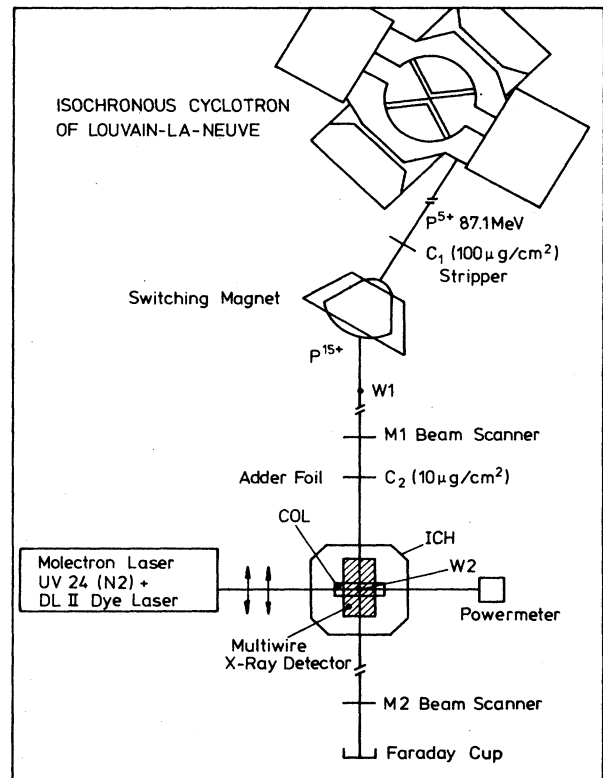

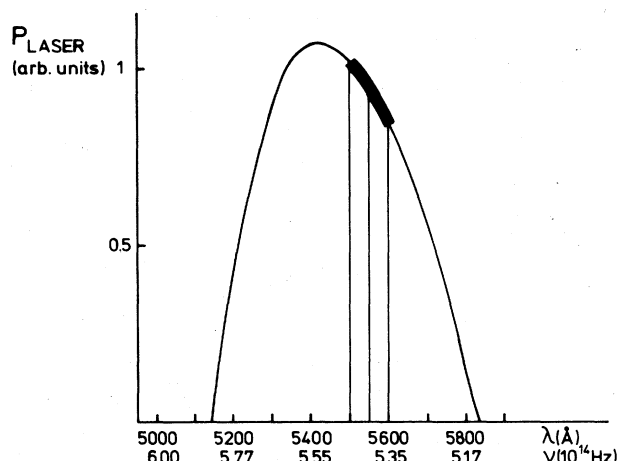FIG. 2. General scheme of the experimental setup. Detailed view of the ion-beam trajectory.

FIG. 3. The measured-power response function of the coumarin C495 dye as a function of the laser-output wavelength (or frequency), in arbitrary units. The region of the curve to be explored is also indicated.

with the laser. On the other hand, the laser light was focused to a spot of 1 mm in diameter and interacted with the ion beam at 90° with respect to its direction as shown in Fig. 2. The laser beam, crossing the interacting chamber (ICH) from side to side, was monitored in a standard power meter purchased from Scientech Inc.[29]

A fast multiwire gas $(Ar-CH_4-C_2H_2)$ counter with a large solid angle was placed on the top of the ICH to detect the induced x rays (2.3 keV) through a Kapton[30] foil of 12μ thickness. A Faraday cup, placed at the end of the beam tubes, was used to monitor the total beam current in order to normalize the different measurements.

As the phosphorus beam was delivered in a pulsed mode with a burst duration of 5 ns FWHM and a repetition rate of 12.02 MHz (cyclotron radio frequency rf), and as the laser beam also has a pulsed structure with a maximum repetition rate of 50 Hz and a time structure of 7 ns FWHM, one of the major experimental difficulties of our setup was to achieve an absolute phase synchronization between these two beams to give a maximum overlap at the point subtended by the x-ray detector. These requirements implied a continuous control of the time reference

chosen to synchronize the two beams. For this purpose two removable tungsten wires were used ($W1$ and $W2$ in Fig. 2), viewed by two detectors (plastic scintillators coupled to a photomultiplier) detecting either scattered ion and/or scattered laser light, as will be explained in a subsequent paragraph.

B. Laser spectrum

Our laser system was a commercial Molectron device[31] composed of (a) an UV24 pulsed nitrogen laser (peak power 1 MW), maximum repetition rate of 50 HZ, pulse duration 10 ns) and (b) a grating-tuned dye laser with a DL14 amplifier, delivering light pulses of 7 ns FWHM pumped by the UV24 nitrogen laser. The nitrogen laser is not the familiar optical feedback amplifier operating on the basis of the stimulated emission, but rather a source of spontaneous emission of radiation arising from many atoms emitting coherently. This phenomenon, bearing the name of superradiance, is the quantum electrodynamical counterpart of the well-known N emitter effect. When N emitters are properly phased, they interfere constructively with each other giving an emission rate proportional to N^2. The laser emission centered at 3371 Å is produced by a very fast high-voltage discharge. As the lifetime of the upper laser level is only 40 ns and as the laser transition feeds a metastable level, the laser operates only in a pulsed mode. The pulse duration was limited to about 10 ns. In this type of laser the use of mirrors at both ends of the cavity is not necessary, and they are only used to enhance the superradiant output. The dye used to explore the resonance was coumarin C495 dissolved in ethanol to a concentration of 10^{-2}. The dispersive element of the dye laser was a grating of 600 lines per mm blazed at an angle of $54°6'$. Without telescope, the total bandwidth achieved (3 Å) was sufficiently narrow to explore the full resonance (50 Å). Figure 3 shows, in arbitrary units, the measured-power response function of the dye as a function of the output wavelength. The peak power at maximum efficiency was 100 kW.

The wavelength calibration of the dye laser was achieved by means of a spectrometer of the Ebert-Fastie type with two fixed apertures and a focal distance $f = 3.52$ m, as shown in Fig. 4. The laser wavelength
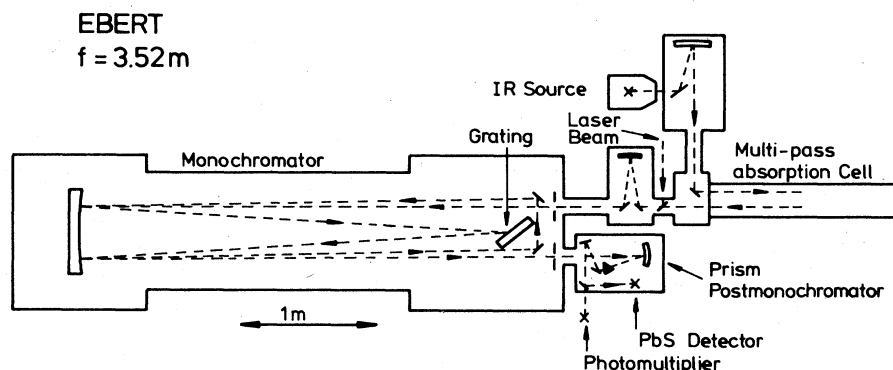

FIG. 4. General scheme of the high resolution Ebert-Fastie monochromator used for the laser wavelength calibration.
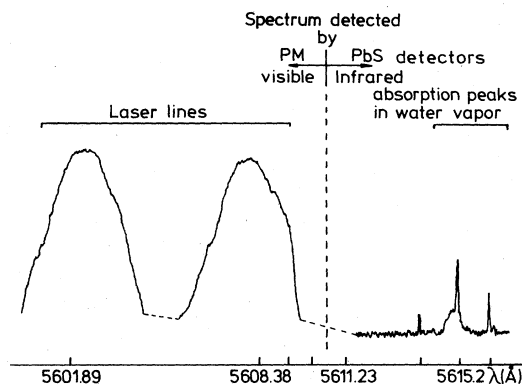
FIG. 5. Two typical laser lines at different grating positions, measured using our monochromator. It shows a superposition of the laser-output spectrum and some infrared absorption peaks in water vapor as a function of their wavelengths. Using these narrow absorption peaks as references, the laser lines are determined to an overall accuracy of 0.4 Å.

calibration was performed in the following way. The laser beam was transported from our experimental area to the spectrometer, a distance of 300 m, using an acrylic optical fiber; the laser light, focused onto the entrance aperture, was reflected by a spherical mirror, then dispersed by a grating and reflected back to the spherical mirror inducing a second passage on the grating before focalizing the light onto the output aperture; the scanning of the wavelength was done by rotating the grating, with an auxiliary prism post monochromator separating the wavelengths of the different orders of diffraction; the light injected in the spectrometer was alternately the laser light or the infrared radiation from a carbon filament at high temperature. In the former case the lines were detected with a photomultiplier, while in the latter, the absorption peaks of the light in the residual water vapor in the infrared region were detected with a PbS detector.

The calibration consisted of taking *simultaneously* a spectrum of the laser line (diffraction order 45) and several well-known absorption peaks in water vapor (order 9). Figure 5 presents a typical superposition of two such spectra as a function of wavelength (Å). Using the narrow absorption peaks as references, the laser line was determined to an overall accuracy of 0.4 Å.

C. Synchronization of the pulsed laser output with the beam bursts of the cyclotron

As we mentioned previously, the ion and the laser beams were delivered in a pulsed mode. In order to synchronize these two beams, three technical conditions had to be achieved: (a) a proper cyclotron rf-beam burst phase-shift correction,[32] (b) a perfect stabilization of the light-output delay of the nitrogen laser with respect to an external trigger pulse,[33] and (c) a maximum overlap of the two beams in the region subtended by the x-ray detector taking into account the velocity difference of the ions and the laser radiation.[34] In fact, any time difference equivalent to 10 ns or more between the two beams, can-

cels the probability of inducing any resonant transition between the $2s_{1/2}$ and $2p_{3/2}$ states in hydrogenic phosphorus. This probability, given by the convolution of the temporal shapes (quasi-Gaussians) of the ion pulse and the laser-light pulse, decreases by 10% (20%) if the time difference is about 1.7 ns (2.4 ns).

Therefore we had, in the first stage, to develop a new type of time-reference signal always in phase with the cyclotron beam bursts. The most simple and realistic time-reference signal would have been the cyclotron rf pulse delivered by the synthesizer at each beam burst. However we found that this approach remains unsatisfactory for experiments in the nanosecond range due to their slow relative phase drift. An rf-beam burst phase-shift corrector was developed. This was achieved[32] by coupling the usual rf signal to a typical scintillator time-pickoff assembly viewing the ion beam diffused by the $W1$ tungsten wire after the switching magnet (see Fig. 2). This wire was viewed by a plastic scintillator (NE-102A), 2 mm thick, coupled to a 56AVP Philips photomultiplier tube through a Plexiglass light pipe used as a vacuum seal, the phototube being in air. By feeding the rf signal and the anode signal of this scintillator assembly to the homemade phase-shift corrector working in a sampling mode, it delivered with 100% efficiency a reconstructed rf signal (RRF) always in phase with the ion burst, independent of any modification or drift in the operating conditions of the cyclotron. The correction was limited to 0.1 ns per pulse to avoid excessive response to noise pulses from the detector. The block diagram of this phase-shift corrector has been described in detail elsewhere;[32] we comment here only on the performance of this setup (Fig. 6). The data in Fig. 6(b) illustrate a simulated slow phase drift ($\sim$20.3 ns overall FWHM between the rf signal and the beam bursts in normal running of the cyclotron, while the data
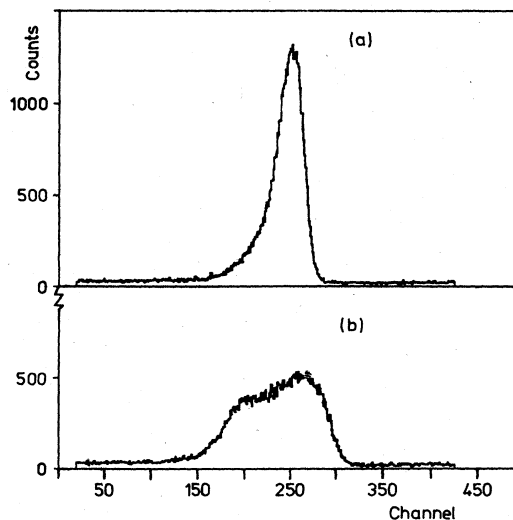

FIG. 6. Two time spectra (TAC) illustrating (a) the improvement (FWHM=5.9 ns) when the rf pulse is derived from the phase-shift corrector device and (b) the slow phase drift (FWHM$\sim$20.3 ns) between the radio-frequency (rf) signal of the cyclotron and the beam bursts in normal running of the cyclotron.

in Fig. 6(a) show the improvement (5.9 ns) when we used the rf—phase-shift-corrector device and the derived RRF as the time-reference signal. If one takes into account the instrument response function in these measurements, one can conclude that we achieved a phase-drift correction much better than 1 ns by using the new defined RRF signal.

In a second stage of our investigations we found that the time delay of the laser-light output with respect to an external trigger was not constant as per the commercial specifications, but subject to a slow and large drift (25 ns is the best we could achieve for a short time running without regulation) greatly exceeding the width of the ion burst (3—5 ns) and the specified jitter (± 1 ns). Such a drift was electronically corrected by means of a feedback system (composed of a fast detector of the laser-light pulse coupled to an automatically adjustable external delay in the trigger circuit of the laser) and by taking into account the measured delay between the trigger pulse and the light output in the previous firings. This electronic circuit will be called, in the following, the "laser phaser." Complete details of this arrangement are described elsewhere.[33] As it is shown later in a more general electronic diagram (see Fig. 11), the RRF reference signal was fed into the phaser as well as the trigger signal (derived from the cyclotron heavy-ion source). The N_2 laser was started with a pulse delivered by the phaser using an optical coupling in order to avoid any disturbance of the phaser by the EMI noise picked up in the wires during the discharge of the laser. Part of the light output, suitably attenuated,

Channel   (a)
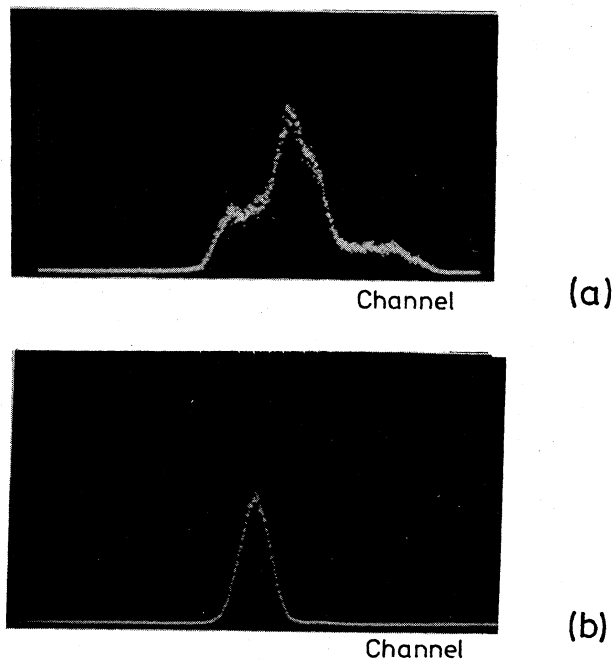

Channel   (b)

FIG. 7. Two time spectra (TAC) illustrating (a) the phase drift (FWHM=24 ns) between the laser-light output and its externally triggered signal and (b) the improvement (FWHM=1.85 ns) when the laser is triggered by the "phaser electronic device allowing almost a 90% temporal overlap between the ion and laser beams.

was detected by a silicon avalanche photodiode (RCA-type C-30902-E). The pulse, shaped by fast electronics, was fed back into the phaser for comparison with the RRF signal (time reference) and for the dynamical correction of the delay of the next trigger of the laser. Figure 7(a) shows the measured time relationship between the laser output and the trigger with the phaser disconnected. This figure clearly shows that the total width of the spectrum (24 ns) over 2500 s of running greatly exceeds the width of the ion burst. When the laser was triggered with the phaser we obtained the spectrum displayed in Fig. 7(b) for a running time equivalent to Fig. 7(a) [Fig. 7(b) is extended by a factor of 2 as compared to Fig. 7(a)]. The phaser reduces the width of the time spectrum from 24 ns to 1.85 ns FWHM. With this arrangement almost 90% of the light pulses occurred within 2 ns, allowing a good temporal overlap of the ion burst and the laser light.

In the third stage of our experimental setup the *absolute* synchronization between the laser and ion beams was fixed in such a way that they always crossed each other at the point subtended by the x-ray detector. This was achieved by introducing a tungsten wire ($W2$, see Fig. 2) at the desired crossing point and by *alternately* detecting the elastically scattered phosphorus ions and the scattered laser light with a detection system[34] similar to the time-pickoff assembly used for the cyclotron rf-beam burst synchronization. The time relation between these two scattered beams with respect to the RRF signal should be the same taking into account the velocity difference of the ions and the light pulse (2.8 ns). If not, one manually corrected (additive cable) the delay of the RRF signal (see Fig. 11) fed into the laser phaser until perfect synchronization was achieved. After this adjustment the wire ($W2$) was removed. This absolute synchronization was monitored continuously by measuring the time relationship between the time-pickoff assembly viewing the ion beam at the first tungsten wire ($W1$) and the signal derived from the silicon photodiode detecting part of the laser-light output. The arbitrary time interval between these signals must remain constant during the measurements.

D. Monitoring of the cross angle of the laser and the ion beams

An important Doppler shift affects the wavelength of the laser light in the rest frame of the moving ion with velocity $\beta = v/c = 0.0767(2)$. If the crossing angle of the two beams is defined by θ, the relative wavelength Doppler shift is given by

$$\frac{\Delta\lambda}{\lambda_0} = \frac{\lambda - \lambda_0}{\lambda_0} = \gamma(1 - \cos\theta) - 1 , \qquad (27)$$

where λ is the wavelength of the light emitted by the laser (Lab.), λ_0 is the corresponding value in the rest frame of the moving phosphorus ion, and $\gamma = (1 - \beta^2)^{-1/2}$.

If the crossing angle $\theta = \pi/2$ and $\lambda_0 = 5560$ Å (about the theoretical centroid of the resonance), one finds a transverse Doppler shift of $\Delta\lambda = 16$ Å. This value drops to zero ($\lambda = \lambda_0$) at 87.8°, clearly illustrating the sensitivity of our experiment with respect to the angle θ. This sensi-

tivity can be written as

$$\left|\frac{\partial\lambda_0}{\partial\theta}\right| = \lambda\frac{\beta}{\gamma}\frac{\sin\theta}{(1-\beta\cos\theta)^2} \ . \tag{28}$$

It is maximum at $\theta\cong 81°28'$ and zero at $\theta=0°$ or $180°$. At $\theta=\pi/2$, $\partial\lambda_0/\partial\theta=0.43$ Å/mrad (for $\lambda=5560$ Å). The uncertainty in λ_0 due to the errors in the determination of λ, θ, and β is given at $\theta=\pi/2$ by

$$\left[\frac{\sigma_{\lambda_0}}{\lambda_0}\right]^2 = \left[\frac{\sigma_\lambda}{\lambda}\right]^2 + (\beta\theta)^2\left[\frac{\sigma_\theta}{\theta}\right]^2 + (\beta\gamma)^4\left[\frac{\sigma_\beta}{\beta}\right]^2 \tag{29}$$

and indicates its negligible dependence on σ_β owing to the fact that $(\beta\gamma)^4\ll 1$. The natural width of the resonance Γ_{nat} is also modified by the Doppler effect because the ion beam is not perfectly parallel and hence possesses a non-vanishing velocity component in the laser-beam direction. In these conditions the total width of the resonance Γ can be written as

$$\Gamma = \Gamma_{nat}\left[1+\left[\frac{\Gamma_D}{\Gamma_{nat}}\right]^2\right]^{1/2} , \tag{30}$$

where Γ_D is the Doppler broadening and $\Gamma_{nat}=5.03\times 10^{12}$ Hz or 51.8 Å (see Table V). As will be shown below, the maximum horizontal divergence of the ion beam at the crossing point is 25 mrad, so that $\Gamma_D=25$ mrad$\times 0.45$Å/mrad$=11$ Å. Therefore, with the total width of the resonance $\Gamma=53$ Å and $\Delta\Gamma=\Gamma-\Gamma_{nat}=1.2$ Å, the resonance shape could be kept as a Lorentzian form.

The inhomogeneities of the spatial structure of the phosphorus beam can also slightly shift the centroid of the resonance. This effect is taken into account when the overall beam direction is given by the center of gravity of its spatial distribution, as discussed in what follows.

In order to minimize the error in our results due to any poor evaluation of the crossing angle of the two beams, it was of great importance to have a perfect alignment procedure for the two beams and a very efficient control system during the experiment. Therefore two reference axes must be defined in space which cross each other at 90° at the point subtended by the x-ray detector. Once these axes were defined, both laser and ion beams had to be made to conform with them. We chose the ion-beam direction as one of the reference axes, and controlled very precisely any displacement from its initial direction. Then the laser light was brought to cross at 90°.

Any usual techniques to visualize an ion beam (for example, the aluminum silicate) do not have the required sensitivity nor the linearity to restore the beam inhomogeneities. Therefore we developed a very sensitive system capable to visualizing the exact profiles of the beam, which gave its centroid values with a remarkable precision and allowed feedback corrections of any deviations from an initially adopted direction.[28] This system was composed of two dual grid-type beam scanners placed before and after the crossing point of the ion and laser beams (M1 and M2 in Fig. 2). Each scanner was a dual grid of 48 horizontal and 48 vertical wires, each of 200 μm diam and spaced 1 mm apart on both sides of a printed circuit

board of 1.6 mm thickness covering an aperture of 5×5 cm^2. The printed circuit and the associated electronics were fixed on an X-Y translator table allowing precise positioning in the beam trajectory. The current collected on each wire charged a capacitor, and at regular time intervals the accumulated charge was readout by a microprocessor which also transfers the data to a microcomputer (DAI personal computer). The readout was used to visualize simultaneously the horizontal and vertical profiles of the beam on the screen of an oscilloscope. The microcomputer allowed repetitive and automatic determination of the center of gravity of the beam spatial distribution in a few seconds. If a position drift in the beam direction (≥ 1 mrad) was registered, the computer modulates the current in a correcting steering magnet positioned on the beam line, maintaining the initial axis of the beam (the axis of reference).

By means of this system the centroid of the beam spot was determined with an accuracy of 5×10^{-2} mm, representing the standard deviation of 60 profile measurements at 30 s intervals each. The two beam scanners, positioned symmetrically on both sides of the crossing point at a relative distance of 2 m, allowed the determination of the crossing angle with an accuracy of 0.035 mrad.

The alignment and the determination of the reference axis of the laser beam at $\theta=\pi/2$ with respect to the ion-beam direction was carried out with a He-Ne laser following the experimental procedure shown in Fig. 8. The He-Ne laser beam was positioned to coincide with the ion-beam axis (reference axis), materialized by the center of the two beam scanners, each of which was geometrically centered with the beam tube inside the quadrupoles.

At the given crossing point, a thin semitransparent mirror was positioned on a horizontal goniometer coupled to a stepping motor with sensitivity of $\frac{1}{100}$ of a degree. The "zero" position of the goniometer was obtained by backward reflexion of the He-Ne laser light and the mirror then turned by an angle of 45° to reflect the light at 90° with respect to its incident direction. The dye-laser-beam reference axis was completely determined by reflecting this He-Ne beam with a fixed mirror at 180° through two narrow diaphragms (D), separated by 1.5 m and situated
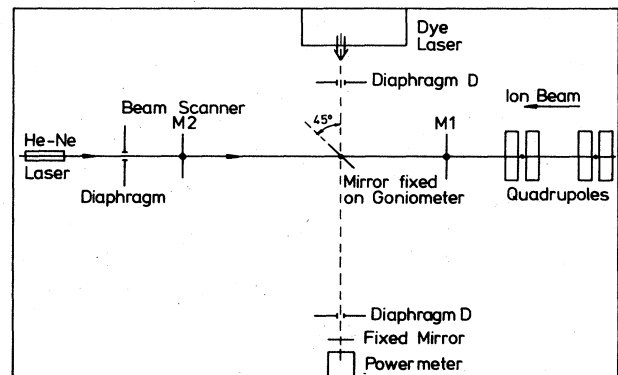

FIG. 8. Schematic of the experimental procedure and setup for the alignment and the determination of the reference axis of the laser beam with respect to the phosphorus-beam direction.

on each side of the crossing point. All optical elements and the power meter were sealed on a standard optical bench. The latter mirror was positioned by reflecting the laser spot back to its origin using the semitransparent mirror already at the 45° position. The dye laser was then mechanically positioned for maximum transmission of the laser power, as monitored by the power meter through these two diaphragms.

In conclusion, the following angular uncertainties are to be associated with the above alignment procedure: 0.10 mrad due to the zero positioning of the goniometer; 0.35 mrad associated with the rotation at 45° of the semitransparent mirror; 0.10 mrad in the positioning of the fixed mirror; 0.15 mrad in the positioning of the diaphragms; 0.10 mrad in the positioning of the ion-beam scanners; 0.15 mrad in the positioning of the dye laser, and 0.035 mrad in the determination of the ion-beam direction. Therefore the total uncertainty on the crossing angle is expected to be 0.45 mrad, corresponding to an error in the laser wavelength at the resonance centroid of 0.19 Å to be combined with the statistical uncertainty.

FIG. 9. Time distribution (TAC spectrum) registered between the x-ray detector (~2 keV atomic lines) and the cyclotron radio frequency. Typical time resolution of 30 ns (FWHM) and 65 ns (FWTM) can be extracted.

E. X-ray detector

In order to enhance the signal-to-background ratio it was necessary to develop[35] a fast low-energy x-ray detector capable of resolving the successive ion burst of the cyclotron, thus possessing a response time shorter than the rf period of the cyclotron (83.2 ns in this case). This detector also had to fulfill the following requirements: (a) large solid angle and area, (b) 100% intrinsic efficiency at low energy (~2 keV), (c) compact geometry in order to fit adequately in the complex experimental setup discussed previously, and (d) insensitivity to the EMI (radiated electromagnetic) noise induced by the cavity discharge (30 kV$-$10 ns) of the neighboring N_2 laser. After extensive studies it appeared that all these requirements could be achieved by a fast gas-filled multiwire counter using a high drift-velocity gas mixture[36] of Ar (80 vol %), CF_4 (5 vol %), and C_2H_2 (15 vol %). These conditions correspond to an electron drift-velocity of 0.07 mm/ns at $E/P \geq 1$ V/cm^{-1} Torr^{-1}, where E is the electric field and P the gas pressure. The measured energy resolution was about 25% at 5.95 keV. A detailed description of the detector has recently been published.[35] We give here only the essential features.

The detector we designed is a multiwire-multiplane detector built from 14 anodic grids alternately piled up with 14 cathodi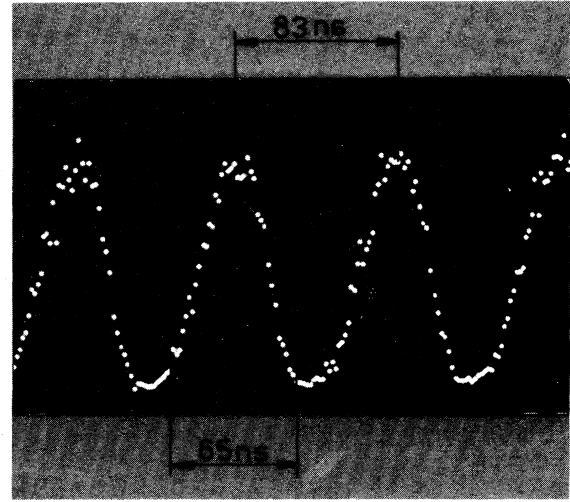c grids. Each grid was composed of 20 parallel goldplated tungsten wires of 20 μm diam, spaced 2 mm apart and perpendicular to the x-ray incidence direction. The anodic and cathodic wire planes were spaced 2.5 mm apart.

The detector's entrance window was a 6 μm thick (50×110 mm^2) aluminized Mylar foil glued to the aluminum body of the detector by an electric varnish to ensure grounding. An additional 29th grounded grid ended the useful region of the detector on the opposite side to the entrance window, ensuring a smooth electric field variation at the detector end. The 20 parallel wires of each grid were soldered on a printed circuit made of epoxy with internal dimensions of 40×110 mm^2. The gas mixture flowed within the detector at a pressure slightly higher than 1 atm.

The usual high voltage applied to each cathodic grid was -2.500 V. The signal was collected separately on each anodic grid coupled to an incorporated individual dual wire chamber discriminator hybrid circuit.

A typical time-resolution spectrum generated by a time-to-amplitude converter (TAC) is shown in Fig. 9. The start pulse was given by the counter detecting the 2.1 keV atomic x ray emitted by the phosphorus beam. The stop pulse was derived from the cyclotron radio frequency (RRF) properly scaled down to observe several successive

TABLE VI. The properties of interest to the background study.

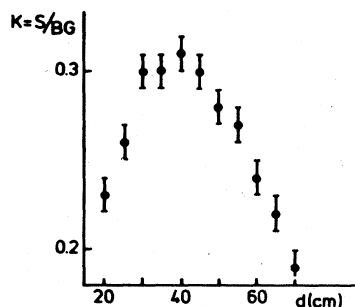| Charge state	Initial atomic state (x-ray multipolarity)	Final state	x-ray energy (keV)	Transition lifetime (cm)
P^{14+}	$2s_{1/2}(2E1-M1)$	$1s_{1/2}$	2.3	24
P^{13+}	$2 {}^1S_0(2E1)$	$1 {}^1S_0$	2.10	17
	$2 {}^3P_2(M2)$	$1 {}^1S_0$	2.14	8
	$2 {}^3S_1(M1)$	$1 {}^1S_0$	2.12	3200
P^{12+}	$2 {}^4P_{5/2}(M2-\text{Auto})$	$1 {}^2S_{1/2}$	2.11	4

FIG. 10. X-ray signal (S) to background (BG) experimental ratio as a function of the second adder-carbon foil distance (d) to the laser-ion-beam interaction region. It is clear from this curve that the recommended distance should be around 40 cm.

beam bursts. It is clear that the achieved time resolution at 2.1 keV is better than the 83-ns rf period (time interval between two successive peaks in the TAC spectrum). More precisely, the measured time resolution was 30 ns at FWHM and 65 ns at FWTM, in excellent agreement with Christophorou et al. estimates.[36]

V. BACKGROUND STUDIES

By means of the well-known beam-foil technique, we determined the optimal conditions for the production of hydrogenlike phosphorus ions as compared to the other charge states. Taking into account the total number of the produced ions, these optimal conditions implied:[24-27] (a) a beam energy of 87.1 MeV P^{5+} ions; (b) a first stripper carbon foil C_1 (see Fig. 1) of 100 $\mu g/cm^2$ thick producing the charge-state distribution $P^{12+}=0.21$,

$P^{13+}=0.43$, $P^{14+}=0.26$, and $P^{15+}=0.040$; (c) a second carbon-adder foil C_2 of 10 $\mu g/cm^2$ (Fig. 2) upon which only bare P^{15+} were made incident to give the final charge-state distribution $P^{12+}=0.08$, $P^{13+}=0.31$, $P^{14+}=0.44$, and $P^{15+}=0.16$.

With these conditions we favored the hydrogenlike charge state as compared to the heliumlike and lithium-like ions which emit background x rays of energy close to the 2.3-keV Lyman-α x rays used to monitor the resonant transition.

Moreover, in order to enhance the signal-to-background ratio we had to choose very carefully the distance between the second carbon-adder foil and the crossing point with the laser beam. Table VI shows the properties of interest of the background studies.

The optimum carbon-foil—crossing-point distance was defined as the interdistance where the ratio of the two-photon contribution from the $2s_{1/2}$ level to the other x rays was maximum. This was extracted from a total decay curve by a special technique explained in Ref. 26. From Fig. 10 it is clear that the crossing point should be at about 40 cm from the adder foil.

VI. DATA ACQUISITION SYSTEM

The data acquisition electronics was very simple and is detailed in Fig. 11. The fundamental device in this setup was the laser phaser, whose functions have been previously described (see Sec. IV). The data to be analyzed were time-to-amplitude spectra registered on a multichannel analyzer (MCA). The phaser was fed by three signals: (a) the cyclotron RRF signal in synchronization with the ion beam bursts, (b) a near 50 Hz trigger signal in phase with the ion-beam source of the cyclotron, and (c) the silicon
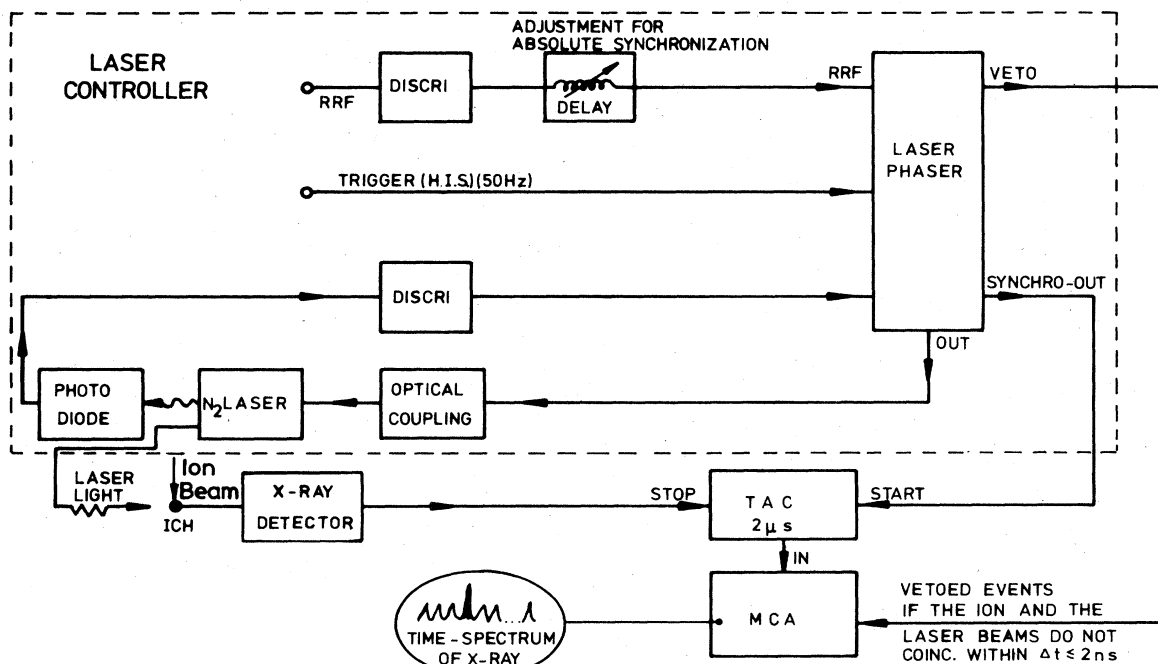

FIG. 11. General scheme of the data acquisition electronics. It details the "laser controller" system.
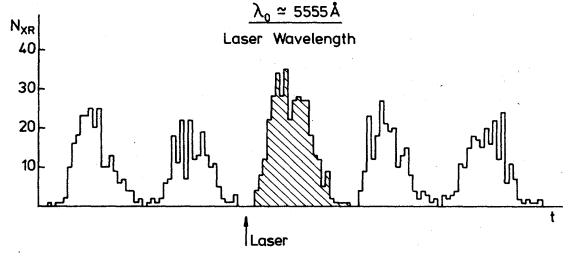
FIG. 12. Partial and typical time-to-amplitude spectrum (TAC) between the x-ray detector and the radio frequency of the cyclotron. This spectrum shows clearly the burst hit by the laser tuned at $\lambda_0 \cong 5555$ Å, the predicted resonance wavelength. The shadowed peak corresponds to an excess counting of 70% in comparison to the other peaks (background contributions).

photodiode signal which detects part of the laser light.

The phaser controlled, with these three signals, the opportune time for triggering the laser by taking into account the eventual drift of the light-output delay using the RRF as an ideal structured-time reference. The synchronized output of the phaser triggered the laser by means of an optical coupling (Hewlett-Packard optical coupler HP 2601) which protected the phaser from any EMI noise.

The phaser also delivered a "synchro-out" pulse five RRF cyclotron periods before the laser trigger was delivered. This signal started a time-to-amplitude converter unit (TAC) which was stopped by the x-ray detector signals. The TAC time range of 2 μs allowed the observation of more than 20 ion beam bursts after the synchro-out signal, and thus simultaneous and accurate measurement of the background contributions in the experiment (see Sec. V). The phaser also delivered a so-called "veto" signal whenever the light pulse was more than 2 ns out of phase, which vetoed the registration of the whole time spectrum. Three types of normalization were then applied to the data (background subtracted) at the different laser light wavelengths: (a) the total beam
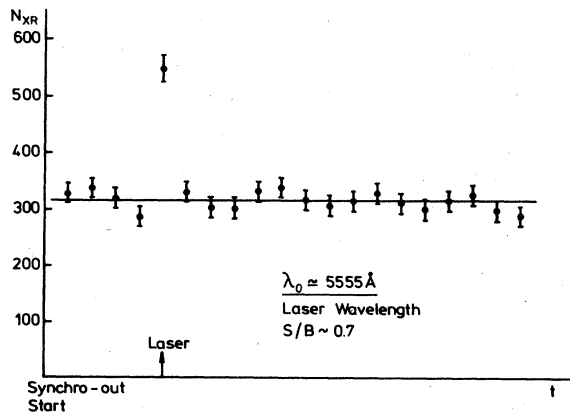
FIG. 13. Integrated x-ray counting of 20 successive ion bursts as a function of time after triggering the electronics (synchro-out). Each point is separated from the next by 83 ns (cyclotron rf period). The burst hit by the laser light shows an excess counting of 70% as compared to the background (fitted full line) (see text and Fig. 12 for more details).

current collected in the Faraday cup, (b) the mean laser power monitored by the power meter, and (c) the number of synchro-out pulses not veted by the phaser, i.e., the number of laser flashes accepted during the experiment.

VII. EXPERIMENTAL RESULTS

Figure 12 shows a time-to-amplitude spectrum limited to 5 (of 20) successive ion bursts, where one sees clearly that the burst hit by the laser at $\lambda_0 \cong 5555$ Å has an appreciable counting excess. Figure 13 shows the integrated x-ray counts in each of the 20 successive peaks as a function of the time interval separating these ion bursts (83 ns). The burst hit by the laser light with the predicted resonance wavelength shows a 70% excess number of counts in comparison to the background contributions. These results demonstrate the performance of our experimental setup.
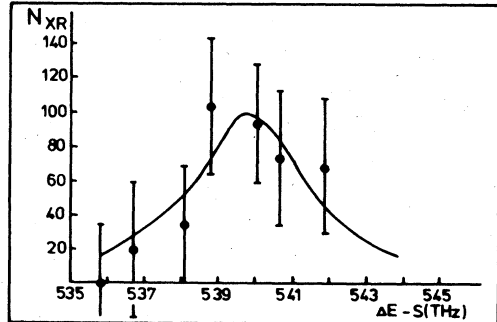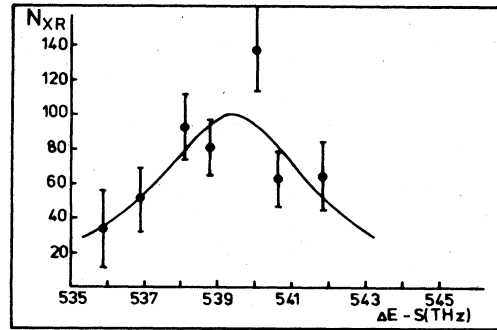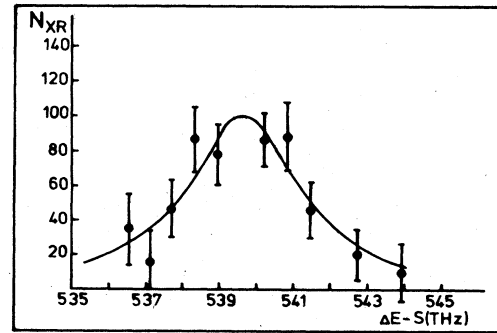

FIG. 14. Three resonance curves registered at similar experimental conditions. They represent the induced x-ray counting as a function of the laser light frequency normalized to the laser power and the ion-beam intensity. The full curves correspond to χ^2 best fits with a Lorentzian shape (see Table VII for the extracted parameters). The curves have been normalized to 100.

TABLE VII. Results of the χ^2 best fits by Lorentzian shape of the three measured resonances. The result of the first resonance is the previously published one, but corrected for a more accurate laser wavelength calibration.

Resonance	Centroid	Stat. error	Doppler effect	Calib. error (THz)
1	539.65	±0.23	±0.08	±0.04
2	539.41	±0.37	±0.02	±0.02
3	539.86	±0.65	±0.02	±0.02
Mean value		539.60(20) THz or 5555.8(2.0) Å		

Figure 14 shows the three resonance curves we registered at similar experimental conditions. The full line curves correspond to a χ^2 best fit of a Lorentzian shape with three free parameters (the amplitude, the width, and the centroid). Table VII details the results of these fits, together with the contributions of the different uncertainties (statistical error, Doppler effect, and laser calibration) discussed previously.

The hyperfine splitting of ^{31}P was estimated to be negligible compared to the width of the resonance and has not been taken into account in the theoretical line shape. The mean value of the resonance frequency $(\Delta E - S)$ is 539.60(20) THz corresponding to a wavelength value of 5555.8(2.0) Å and a precision of 3.5×10^{-4}. Figure 15 shows a *graphic* combination of the three experimental resonances for illustrative purposes only.

Using the experimental value of $\Delta E - S$ one can deduce S, the Lamb-shift contribution, and compare it with the theoretical predictions of Erickson[8] and Mohr.[10] Since the fine structure ΔE is calculated differently by these authors, two different values of S must be extracted from our measurements before any confrontation with the presently available calculations in the framework of QED. Following Erickson's calculations, we have $\Delta E = 559.7067(232)$ THz with $(\Delta E - S)_{\text{expt}} = 539.60(20)$ THz, and $S^E_{\text{expt}} = 20.11(20)$ THz. Following Mohr's calculations, $\Delta E = 559.7302(73)$ THz with $(\Delta E - S)_{\text{expt}} = 539.60(20)$ THz, and $S^M_{\text{expt}} = 20.13(20)$ THz. The

differences between the theoretical and experimental values are 0.43 ± 0.20 THz for Erickson calculations, and 0.12 ± 0.20 THz for Mohr calculations. The deduced value of the Lamb shift is in agreement with Mohr's calculations, although slightly lower, and is more than two standard deviations below Erickson's estimate.

VIII. CONCLUSIONS

For more than 30 years great efforts have been devoted to the measurement of the Lamb shift in hydrogen. When the calculations of both Erickson and Mohr became available, the experimental investigations reached a high degree of sophistication. Beautiful experiments have been carried out reducing the uncertainty to the level of 10^{-6}. This level of accuracy is indeed necessary to separate the two existing theoretical predictions.

Our result is as follows: (i) in agreement with, although slightly lower than, Mohr's calculations, and (ii) more than two standard deviations lower than the predictions of Erickson. In Fig. 16 we display a comparison between theoretical predictions and experimental values of the Lamb shift in the $Z = 15-18$ region. From this confrontation one may conclude that the experimental data drastically diverge from Erickson's calculations and agree to some extent with Mohr's predictions. In fact the data appear to exhibit some general trend of the recent Lamb-shift measurements as compared to Mohr's calculations, indicating systematic deviations as Z increases. We decided to investigate this systematic deviation in more detail by extending the comparison to previous Lamb-shift results in lower Z hydrogenic atoms. Thus Fig. 17 shows in a semi-log plot the differences (D) between theory (Mohr) and the experiment as a function of Z for many atoms $(Z = 1, 2, 6, 9, 15, 16, 17,$ and $18)$.[37−43] Our aim in this comparison is not to extract quantitative information, although we have done a precise fit, but to essentially show that this systematic trend observed in high-Z atoms is also present at lower Z. For clarity we have omitted representing the uncertainties of the experimental data, which in most cases overlap with both Mohr's and Erickson's values. On the other hand, only the most precise available data are displayed in Fig. 17. The Lamb shift values in Li^{2+} and O^{7+} atoms are also omitted because they give a sign difference with theory.

One observes that the points represent a relatively smooth curve as a function of Z. Thus, we fitted these
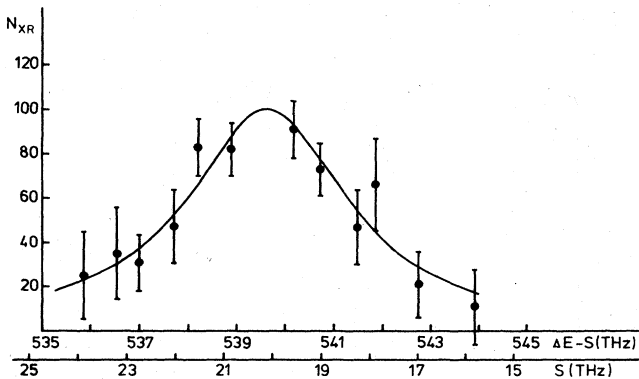

FIG. 15. *Graphic* combination of the three experimental resonances displayed in Fig. 14. It only has an illustrative purpose: no results were extracted from the χ^2 fit.
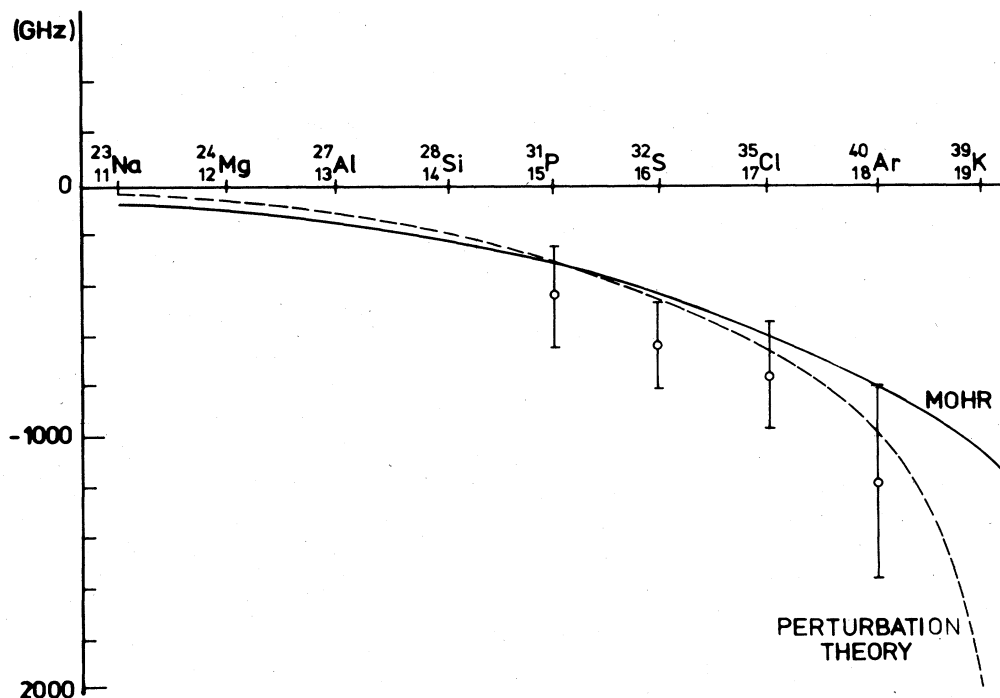
FIG. 16. Comparison between theoretical and presently available experimental values of the Lamb shift. The full curve (Mohr) and the experimental points display the differences with respect to Erickson's calculations. The dashed curve is the difference between the predictions of the series expansion and Erickson's calculations.
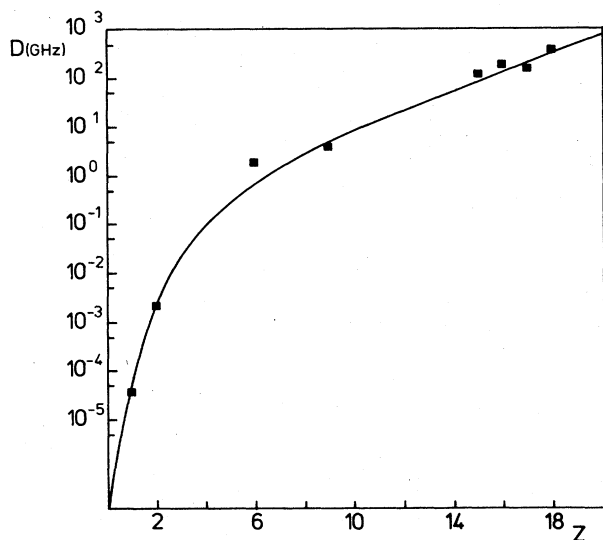

FIG. 17. The differences (D) in GHz between Mohr's calculations and the Lamb-shift experimental values as a function of Z for many atoms $Z=1$ (Ref. 37), $Z=2$ (Ref. 38), $Z=6$ (Ref. 39), $Z=9$ (Ref. 40), $Z=15$ (present work), $Z=16$ (Ref. 41), $Z=17$ (Ref. 42), and $Z=18$ (Ref. 43). The full line curve represents the resulting χ^2 fit to these differences by a $G_{SE}(Z\alpha)$ type of function: $A_0(\alpha Z)^6 + A_1(\alpha Z)^7 + A_2(\alpha Z)^7 \ln(\alpha Z)^{-2}$ (see text for details).

differences with several functions (with constant statistical weight on each point). These functions were of the following general type:

$$A_0(\alpha Z)^6 + A_1(\alpha Z)^7 + A_2(\alpha Z)^7 \ln[(\alpha Z)^{-2}] ,$$

where one or more of the A_i coefficients were set equal to zero. The best χ^2 fit is obtained when all coefficients A_0, A_1, A_2 are kept variable. We must recall that this function represents the interpolation function $G_{SE}(Z\alpha)$ completed by the factorized terms displayed in Sec. II C [Eq. (6)] and in Table II. It has been used by Mohr to calculate the self-energy contribution to the Lamb shift in hydrogenic atoms where specific numerical calculations were not performed. There seems to be thus a tiny but structured difference between Mohr's calculations and the experimental values, suggesting a systematic deviation as a function of Z in the numerical values for $Z = 10, 20, 30, \ldots$.

In order to investigate in more detail the general difference between experiment and theory, it seems to us imperative to extend the Lamb-shift measurement to much higher Z atoms. Such an experiment in hydrogenic krypton ($Z = 36$) has been proposed in Refs. 44 and 45.

ACKNOWLEDGMENTS

---

*Present address: Société Anonyme Belge de Constructions Aéronautiques (SABCA), Chaussée de Haecht, 1470, B-1130 Brussels, Belgium.

†Present address: Stratec, Av. P. de Lorraine 26, B-1410 Waterloo, Belgium.

[1] P. Pellegrin, Y. El Masri, L. Palffy, and R. Prieels, Phys. Rev. Lett. 49, 1762 (1982).

[2] F. Guerin, Cargèse Lectures in Physics, edited by X. Levy (Gordon and Breach, New York, 1968), Vol. 2, p. 191.

[3] H. A. Bethe and E. Salpeter, Quantum Mechanics of One- and Two-electron Atoms, in Handbuch der Physik, edited by S. Flügge (Springer, Berlin, 1957).

[4] D. C. Tsui, A. C. Gossard, B. F. Field, M. E. Cage, and R. F. Dzubia, Phys. Rev. Lett. 48, 3 (1982).

[5] H. A. Bethe, Phys. Rev. 72, 339 (1947).

[6] G. W. Erickson and D. R. Yennie, Ann. Phys. (N.Y.) 35, 271 (1965); 35, 447 (1965).

[7] G. W. Erickson, Phys. Rev. Lett. 27, 780 (1971).

[8] G. W. Erickson, J. Phys. Chem. Ref. Data 6, 831 (1977).

[9] P. J. Mohr, Ann. Phys. (N.Y.) 88, 26 (1974); 88, 53 (1974).

[10] P. J. Mohr, Phys. Rev. Lett. 34, 1050 (1975); P. J. Mohr, At. Data Nucl. Data Tables 29, 453 (1983).

[11] P. J. Mohr, Beam-foil Spectroscopy (I), edited by I. A. Sellin and D. J. Pegg (Plenum, New York, 1976), Vol. 89.

[12] P. J. Mohr, Relativistic Effects in Atoms, Molecules and Solids (NATO Advance Study Institute, Vancouver, British Columbia, 1981).

[13] P. J. Mohr, Phys. Rev. A 26, 2338 (1982).

[14] G. G. Simon, F. Borkowski, Ch. Schmitt, and P. W. Walther, Zeit. Naturforschung Teil A35, 1 (1980).

[15] S. R. Lundeen and F. M. Pipkin, Phys. Rev. Lett. 46, 232 (1981).

[16] Y. L. Sokolov and V. P. Yakovlev, Sov. Phys.—JETP 56, 7 (1982).

[17] J. Sapirstein, Phys. Rev. Lett. 47, 1723 (1981).

[18] E. H. Wichmann and N. M. Kroll, Phys. Rev. 101, 843 (1956).

[19] G. Drake and R. Grimley, Phys. Rev. A 11, 1614 (1975).

[20] B. Curnutte, C. Cocke, and R. Dubois, Nucl. Instrum. Methods 202, 119 (1982); G. Drabe, S. Goldman, and A. van Wijngaarden, Phys. Rev. 120, 1299 (1979).

[21] F. A. Parpia and W. R. Johnson, Phys. Rev. A 26, 1142 (1982).

[22] H. W. Kugel and D. E. Murnick, Rep. Prog. Phys. 40, 297 (1977).

[23] A. Di Giacomo, Nucl. Phys. B 11, 411 (1969).

[24] P. Deschepper, Ph.D. thèse IPC-N-8105, Université Catholique de Louvain, 1981.

[25] P. Deschepper, P. Lebrun, J. Lehmann, L. Palffy, and P. Pellegrin, Nucl. Instrum. Methods 166, 531 (1979).

[26] P. Deschepper, P. Lebrun, L. Palffy, and P. Pellegrin, Phys. Rev. A 24, 1163 (1981).

[27] P. Deschepper, P. Lebrun, L. Palffy, and P. Pellegrin, Phys. Rev. A 26, 1271 (1982).

[28] C. Alaime, L. Bonnet, P. Deschepper, L. Palffy, and P. Pellegrin, Nucl. Instrum. Methods 189, 357 (1981).

[29] Scientech Inc., 5649 Arapahoe Ave., Boulder, Colorado 80303.

[30] Formally known as H-film. This material [Polyamide $(C_{22}H_{10}N_2O_4)_n$, density 1.08—1.14 g/cm^3] is approximately 50 times more resistant to radiation damage than Mylar, manufacturer Du Pont.

[31] Molectron Corp., 177 Northwholfe Rd., Sunnyvale, California 94086.

[32] C. Alaime, L. Bonnet, Y. El Masri, R. Holzmann, L. Palffy, and P. Pellegrin, Nucl. Instrum. Methods 195, 429 (1982).

[33] C. Alaime, J. Bertrand, L. Bonnet, Y. El Masri, L. Palffy, P. Pellegrin, and R. Prieels, Nucl. Instum. Methods 207, 423 (1983).

[34] P. Pellegrin, Y. El Masri, L. Palffy, and R. Prieels, Phys. Scri. T 3, 198 (1983).

[35] B. de Callataÿ, Y. El Masri, L. Palffy, and P. Pellegrin, Nucl. Instrum. Methods 1, 224 (1984).

[36] L. G. Christophorou, D. L. Mc Corkle, D. V. Maxey, and J. G. Carter, Nucl. Instrum. Methods 163, 141 (1979).

[37] S. R. Lundeen and F. M. Pipkin, Phys. Rev. Lett. 46, 232 (1981).

[38] A. Novick, E. Lipworth, and P. F. Yerqin, Phys. Rev. A 105, 1434 (1957).

[39] H. W. Kugel, M. Leventhal, and D. E. Murnick, Phys. Rev. A 6, 1306 (1972).

[40] H. W. Kugel, M. Leventhal, D. E. Murnick, C. K. N. Patch, and O. R. Wood II, Phys. Rev. Lett. 35, 647 (1975).

[41] H. D. Strater, L. von Gerdhell, A. D. Georgiadis, D. Mullev, P. von Brentano, J. C. Sens, and A. Pape, Phys. Rev. A 29, 1596 (1984).

[42] O. R. Wood II, C. K. N. Patel, D. E. Murnick, E. T. Nilson, M. Leventhal, M. W. Kugel, and Y. Niv, Phys. Rev. Lett. 48, 398 (1982).

[43] H. Gould and R. Marrus, Phys. Rev. A 28, 2001 (1983).

[44] L. Palffy, Rapport Interne IPC-N-7601, Université Catholique de Louvain (unpublished).

[45] P. Deschepper, Ph.D. Thèse Annexe IPC-N-8105, Université Catholique de Louvain, 1981 (unpublished).
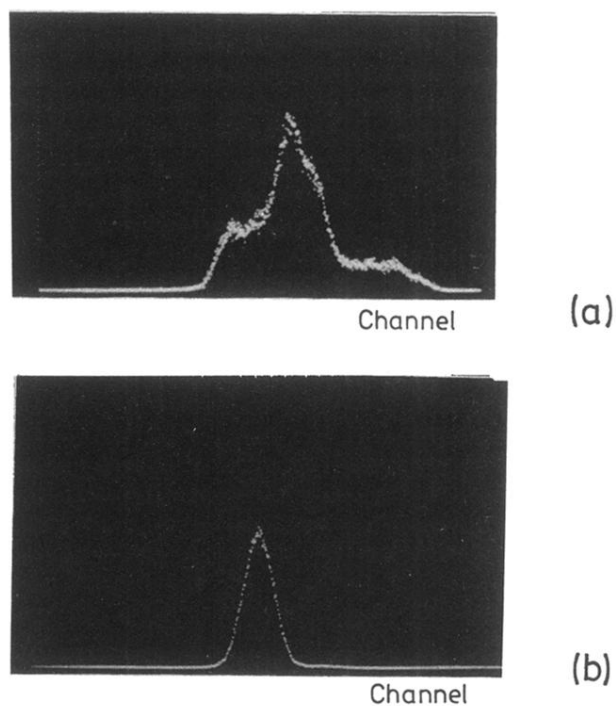
(a)

Channel

(b)

Channel

FIG. 7. Two time spectra (TAC) illustrating (a) the phase drift (FWHM = 24 ns) between the laser-light output and its externally triggered signal and (b) the improvement (FWHM = 1.85 ns) when the laser is triggered by the "phaser electronic device allowing almost a 90% temporal overlap between the ion and laser beams.
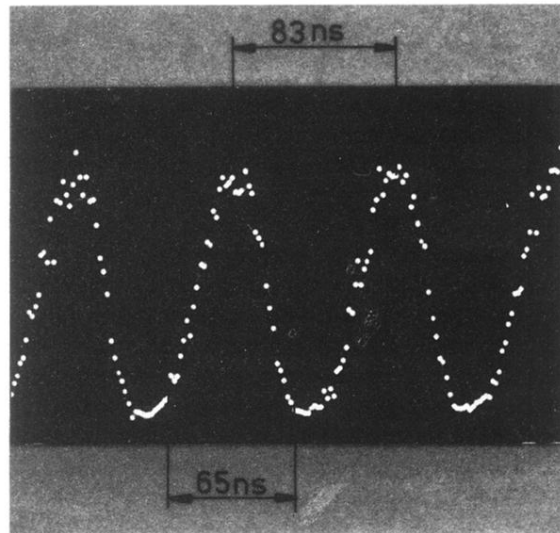
FIG. 9. Time distribution (TAC spectrum) registered between the x-ray detector (~ 2 keV atomic lines) and the cyclotron radio frequency. Typical time resolution of 30 ns (FWHM) and 65 ns (FWTM) can be extracted.